RSC Advances

PAPER

View Article Online
View Journal | View Issue



Cite this: *RSC Adv.*, 2022, **12**, 11923

# The effect of Mn and Co dual-doping on the structural, optical, dielectric and magnetic properties of ZnO nanostructures

Akif Safeen, *[a] Kashif Safeen,*[b] Muhammad Shafique,[a] Yousaf Iqbal,[a] Naveed Ahmed,[a] M. Abdul Rauf Khan,[a] Ghulam Asghar,[a] Khaled Althubeiti,[c] Sattam Al Otaibi,[d] Ghafar Ali,[e] Wiqar H. Shah[f] and Rajwali Khan *[g]

This paper addresses the effect of Mn (2%, fixed) and Co (2, 4, and 6%, varied) substitution on the structural, optical, dielectric and magnetic responses of ZnO nanoparticles synthesized by the co-precipitation chemical route. The X-ray diffraction analysis confirms the hexagonal wurtzite structure of ZnO. The incorporation of co-doping in the ZnO host, indicated by peak shifting in the XRD patterns, enhanced the crystallite size of the Mn/Co dual-doped ZnO nanoparticles. The FTIR spectra show a characteristic peak around 875 $cm^{-1}$ assigned to Zn–O stretching, this validates the formation of the wurtzite structure of ZnO. Raman spectroscopy reveals the characteristic band of the wurtzite structure of ZnO nanoparticles along with coupled vibration modes of Mn/Co with the donor defect states in the doped samples. Enhanced optical absorption in the visible region and a significant red-shift in the absorption band edge were found due to doping. The optical band gap is found to decrease from 3.45 eV to 3.15 eV when Co doping increases up to 6%. The dielectric properties, strongly frequency-dependent, decrease with increasing Co doping while the electrical conductivity increases. Ferromagnetism is observed in all the doped samples, and its origin is attributed to an increase in oxygen vacancies which form bound magnetic polarons. It can be inferred that the doping of Mn and Co can be an effective tool to tune the physical properties of ZnO nanoparticles for potential spintronics and high-frequency applications.

Received 19th March 2022
Accepted 8th April 2022

DOI: 10.1039/d2ra01798a

rsc.li/rsc-advances



## 1. Introduction

Because of the extraordinary qualities and many applications, zinc oxide (ZnO) has piqued the curiosity of many scientists. It has a broad bandgap (3.37 eV) and a high exciton binding energy (60 meV) under ambient conditions,[1] as well as a high piezoelectric constant,[2] and chemical and mechanical stability.[3] Because of its distinct responses, it has the potential to be used in a wide range of applications, including spintronics, photodetectors, solar cells, light-emitting diodes, gas sensors, and photocatalysts.[4,5] Many synthesis techniques, such as co-precipitation, hydrothermal methods, sol–gel methods, wet chemical methods, and chemical vapour deposition, have been used to create ZnO nanostructures.[5,6] Among them, the co-precipitation chemical method is a facile, economical, and valuable synthesis route. It was used in the current report to synthesize ZnO and (Mn, Co) doped ZnO nanoparticles.

Doping in ZnO with transition metal (TM) can effectively enhance the physical properties, particularly optical, dielectric and magnetic. Recently, there have been many reports on room temperature ferromagnetism (RTFM) in TM ions ($Ni^{2+}$ $Co^{2+}$, $Mn^{2+}$, *etc.*) doped ZnO nanostructures.[7] The magnetic ordering and magnetization are exceedingly feeble in these ZnO-based diluted magnetic semiconductors (DMSs). Additionally, the mechanism by which TM doped into ZnO exhibits ferromagnetism (FM) is still contested, and whether it is an inherent or extrinsic property remains unclear. Therefore, the root of RTFM has not been entirely resolved and opened a new path in spintronics research. Identifying the key parameters that govern DMS ferromagnetism remains a significant challenge. The system with intrinsic FM and high magnetic moment at room temperature is the only important factor in realizing the dream of a spintronics device.[8] Therefore, enhancing their magnetic

[a]*Department of Physics, University of Poonch, Rawalakot, AJK 12350, Pakistan. E-mail: akifsafeen@upr.edu.pk*

[b]*Department of Physics, Abdul Wali Khan University, Mardan 23200, KPK, Pakistan. E-mail: kashifsafeen@awkum.edu.pk*

[c]*Department of Chemistry, College of Science, Taif University, P.O. Box 11099, Taif 21099, Saudi Arabia*

[d]*Department of Electrical Engineering, Collage of Engineering, Taif University, P.O. Box 11099, Taif 21944, Saudi Arabia*

[e]*Nanomaterials Research Group, Physics Division, PINSTECH, Islamabad 45650, Pakistan*

[f]*Department of Physics, International Islamic University, Islamabad 44000, Pakistan*

[g]*Department of Physics, University of Lakki Marwat, 28420, Khyber Pakhtunkhwa, Pakistan. E-mail: rajwali@ulm.edu.pk*

properties with suitable and tunable FM and coercivity is essential for potential application as a data storage device. Country to single TM doped ZnO, the simultaneous doping of two TM ions in ZnO is preferable to obtain the best magnetic and optical properties due to the occupancy and adjusted position of the Fermi level.[9] Consequently, the researchers made immense efforts in the TM dual-doped ZnO and studied distinct combinations of TM ions in the ZnO system to accomplish RTFM.[10–12] For instance, it has been reported by Vijayaprasath *et al.* that the RTFM in ZnO nanoparticles is enhanced by the co-doping Ni/Mn, and its origin is attributed to exchange interaction between localized spin-polarized electrons.[13] Intrinsic defects and oxygen vacancies induced the FM at room temperature in Ni–Co co-doped ZnO thin films.[14] The vacancy-associated defect may enhance RTFM response in nanocrystalline co-doped Co/Cu ZnO.[15] Under the optical point of view, ZnO being wide band gap can only be stimulated in the presence of UV light, which covers only 5% of the sun's energy that reaches the earth. In addition, electron–hole pairs of the photo-excited recombine quickly on the ZnO surface, reducing its photocatalytic activity. To address these issues, doping with transition metals is used to improve ZnO optical characteristics and prevent the recombination of electron–hole pairs of light-generated charge carriers.[16] The enhancement in ZnO visible light optical properties can be attributed to the metal ions incorporation in the lattices of ZnO, which slender its band gap and raise the delocalization of electrons in the ZnO nanostructure.[17] Though Co and or Mn-doped ZnO system has been numerously studied, most of them focus on thin films or ZnO nanostructures with limited Co/Mn composition,[18–20] and the detailed investigation of the physical properties of Mn/Co-doped ZnO nanopowders is still inadequate.

An experimental effort has been made to resolve the contradictory issues on the optical and magnetic properties. In the present work, we have simultaneously doped both Mn and Co ions into ZnO to alter the structures and crystalline properties of the host ZnO lattice to obtain the best optical and magnetic response for future application. The most important findings of the current work are narrowing the band gap of ZnO nanostructure from 3.45 eV to 3.15 by Mn/Co doping. Ferromagnetism is found in all doping concentrations, and it is ascribed to an increase in oxygen vacancies, which create bound magnetic polarons. The dielectric characteristics, which are substantially frequency-dependent, drop as Co substitution increases while electrical conductivity improves. It is concluded that Mn and Co doping can be a useful tool for tuning the properties of ZnO nanoparticles for possible spintronics and photocatalytic applications.

## 2. Experimental details

### 2.1 Materials

Sigma-Aldrich provided zinc nitrate hexahydrate [$Zn(NO_3)_2 \cdot 6H_2O$], cobalt nitrate hexahydrate [$Co(NO_3)_2 \cdot 6H_2O$] and manganese nitrate tetrahydrate [$Mn(NO_3)_2 \cdot 4H_2O$], with the purity of 99.99 percent. In addition, sodium hydroxide (NaOH), which was used as a precipitation agent, was also purchased from Sigma-Aldrich. All of the reagents in the experiment were used in the as-received form, with no further purification.

### 2.2 Sample preparation

The co-precipitation method was used to synthesize undoped and (Mn, Co) dual-doped ZnO nanoparticles. Zinc nitrate hexahydrate was dissolved in 100 ml of deionized water, and then 50 ml of the aqueous solution of NaOH (1 M) was applied drop by drop while constantly swirling until a pH of 10 was reached.[21] After the reaction, white precipitates were obtained, washed with distilled water several times in a centrifuge for 10 minutes each to remove contaminants. The obtained precipitates were oven-dried at 80 °C for 10 hours. Lastly, the ZnO nanopowder was heated in a muffle furnace at 600 °C for 2 hours under environmental temperature. A 100 ml solution of zinc nitrate hexahydrate, manganese nitrate tetrahydrate and cobalt nitrate hexahydrate was prepared for Mn and Co dual-doped specimens. A 1 M aqueous solution of NaOH was introduced drop by drop while vigorously swirling until a pH of 10 was obtained. The precipitates were collected and cleaned by centrifugation before being dried in an oven at 80 °C and heated in a furnace at 600 °C for 2 hours. The synthesized samples were labeled as undoped ZnO (pure ZnO), 2% Mn and 2% Co doped ZnO (Mn2Co2), 2% Mn, and 4% Co-doped ZnO (Mn2Co4), and 2% Mn and 6% Co doped ZnO (Mn2Co6).

### 2.3 Characterization

Next, the manufactured samples were analyzed using XRD (PAN analytical) and Cu K radiation, and the lattice constants were obtained using the Rietveld program's GSAS suite. The morphology of the prepared sample was assessed using Scanning Electron Microscopy (SEM, Hitachi S4800, Japan). The chemical composition was measured using Energy Dispersive X-ray Spectrometer (EDAX) attached to the SEM. The functional groups were identified by Fourier Transfer Infrared Spectroscopy (FTIR) in the frequency region 500 to 4000 $cm^{-1}$. The optical properties of the samples were investigated by UV-Vis spectrometer. The dielectric characteristics and conductivities of the sample were determined using a gold terminal pellet in the impedance analyzer in the frequency range of 40–$10^6$ Hz. The magnetic responses were measured through Superconducting Quantum Interface Devices (SQUID).

## 3 Results and discussion

### 3.1 Structural analysis

Fig. 1 demonstrates XRD patterns of the pristine and the dual doped ZnO nanostructures obtained by the co-precipitation route. From these patterns, it can be seen that all samples are polycrystalline. All the specimens have a pure single-phase and crystallize with the hexagonal structure (wurtzite-type $P6_3mc$ space group). The Lattice parameters of $a = 3.2481$ Å, $c = 5.1852$ Å were obtained using Rietveld refinement, (weighted profile factor $R_{WP} = 9.51\%$, and the goodness-of-fit $\chi^2 = 2.572$) for the pure ZnO as shown in Fig. 1(a). The diffraction patterns were indexed well according to JCPDS card no. 36-1451, which

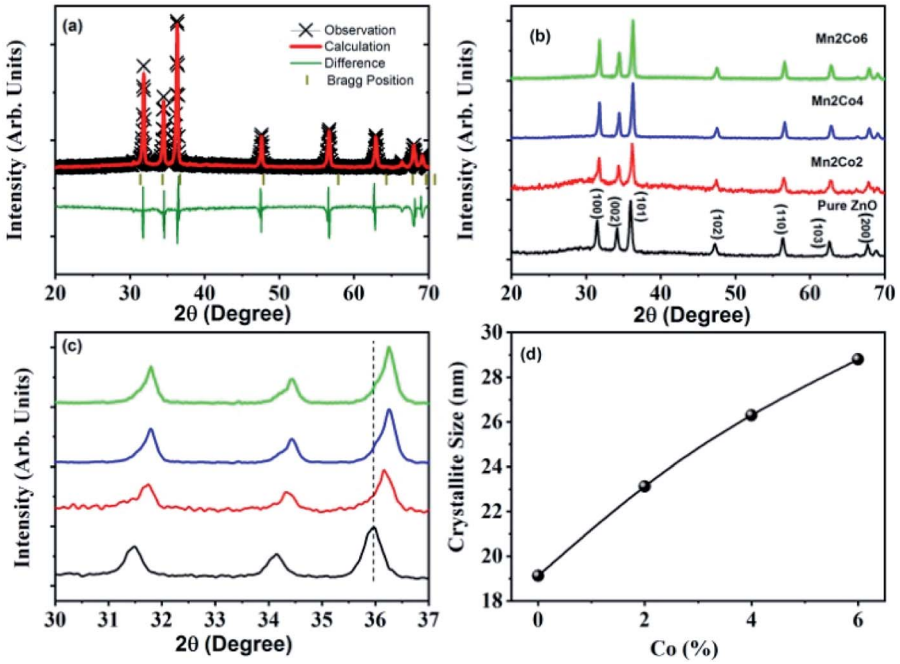


Fig. 1 (a) Shows the solid lines display the Rietveld refinement of the XRD of ZnO nanoparticles, (b) the powder XRD patterns of different doping, (c) the peak shifting with different doping, and (d) the crystallite size of ZnO, and (Co, Mn) dual-doped ZnO.

validates the pure wurtzite phase of ZnO for all synthesized samples, with the diffraction peak corresponding to planes (100), (002), (101), (102), (110), (103) and (200) as shown in Fig. 1(b). Also, there are no extra peaks related to the impurity. It can be seen that there is a relative change in the position of characteristic peak (101) with dopant concentration for all the samples, as shown in Fig. 1(c). This change with dopant concentration confirms substituting dopants ions (Mn, Co) into the ZnO host lattice. The substitution of (Mn, Co) ion into ZnO host material induces lattice distortion, which is due to the difference in the radii of dopant Mn (0.80 Å), Co (0.72 Å), and host Zn (0.74 Å) ions.[22,23]

The lattice parameters $a$ and $c$ and the volume of the unit cell ($V$) of all samples were calculated using the following equations:

$$\frac{1}{d^2} = \frac{4}{3}\left(\frac{h^2 + hk + k^2}{a^2}\right) + \frac{l^2}{c^2} \quad (1)$$

$$V = \frac{\sqrt{3}}{2}a^2 c \quad (2)$$

where $d$ is the interplanar distance and ($h$, $k$, $l$) are the Miller indices. The values of the structural parameters calculated from XRD are listed in Table 1. The unit cell volume was $V = 47.36$ Å$^3$ for pure ZnO and it increased to $V = 47.41$ Å$^3$ (corresponding to $a = 3.2492$ Å, $c = 5.1871$) for lower Mn and Co doped ZnO specimen. In higher Mn and Co doped ZnO, the unit cell volume further increased to $V = 47.48$ Å$^3$ (corresponding to $a = 3.2501$ Å, $c = 5.1910$ Å) and was higher when compared to pure ZnO. This was expected since the ionic radius of $Mn^{2+}$ (0.80 Å), and $Co^{2+}$ (0.72 Å) are different than $Zn^{2+}$ (0.74 Å). Also, it is detected from the XRD patterns that with increasing the concentration of Mn and Co co-dopant in ZnO, the peaks shifted towards higher angle, as shown in Fig. 1(c). This indicates that samples are transferring to disordered form due to Mn and Co doping.

The following Debye–Scherrer's formula was used to determine the average crystallite size $D$ of the synthesized samples from XRD spectra:

$$D = \frac{0.9\lambda}{\beta \cos\theta} \quad (3)$$

where $\lambda$ is the wavelength of incident X-ray, $\beta$ (in radians) is the angular peak width at half maximum, and $\theta$ represents the Bragg's diffraction angle.

Table 1 Crystallite size, lattice parameters and unit cell volume for all for pure and Mn/Co-doped ZnO nanostructures assessed from XRD results

| Sample | ($hkl$) | 2$\theta$ (degree) | FWHM (radians) | Crystallite size (nm) | Lattice constants | | Unit cell volume (Å$^3$) |
|---|---|---|---|---|---|---|---|
| | | | | | $a$ (Å) | $c$ (Å) | |
| ZnO | (101) | 35.97 | 0.456 | 19.12 | 3.2481 | 5.1852 | 47.36 |
| Mn2Co2 | (101) | 36.16 | 0.377 | 23.12 | 3.2479 | 5.1864 | 47.38 |
| Mn2Co4 | (101) | 36.24 | 0.331 | 26.3 | 3.2492 | 5.1781 | 47.41 |
| Mn2Co6 | (101) | 36.26 | 0.303 | 28.8 | 3.2501 | 5.1910 | 47.48 |

The crystallite size calculated from XRD data was found to be 19.01 nm (Fig. 1(d)); which increases to 28.82 nm with the increase of Co-doping concentration up to 6% and can be attributed to the intervention of dopant in the ZnO crystal growth.

### 3.2 SEM analysis

The surface morphology of the synthesized samples, which was studied by SEM, is depicted in Fig. 2(a) and (b). To clarify and understand the crystal growth, only two SEM micrographs of pure and heavily doped ZnO samples (2% Mn and 6% Co) are shown. For the pure ZnO sample, the SEM micrograph shows that particles of the prepared samples are spherical with a large aggregation of small individual nanoparticles and high porosity area as shown in Fig. 2(a). For Mn/Co doped ZnO nanoparticles, it is clearly evident from Fig. 2(b) that aggregation is nearly controlled, and particles show a consistent and uniform morphology with a slightly larger size distribution. The average crystal size of the nanoparticles for pure ZnO was around 70 nm, increasing to around 110 nm as the doping concentration is increased. The particle size rose as the Mn/Co concentration of ZnO increased, which is commensurate with the crystallite size reported from XRD data. The EDX spectrum validates all the selective elements of Zn, Mn, Co, and O (Fig. 2c and d). From the spectra of ZnO nanoparticles, it can be seen that the most abundant element is Zn followed by O. The doping of Mn/Co in ZnO can be reflected from the EDX spectrum. It is clear from the figure that the doped samples contain the expected Mn and Co elements indicating that the prepared samples were free of impurities. The EDX results further confirmed that the compositions of the synthesized samples were nearly in stoichiometric ratio.

### 3.3 FTIR analysis

Fourier Transfer Infrared Spectroscopy (FTIR) was carried out for the identification of functional groups present in prepared samples in the region 500 to 4000 $cm^{-1}$. Fig. 3(a) shows the FTIR spectrum for pure ZnO, Mn2Co2, Mn2Co4, and Mn2Co6 samples. Absorption peaks appeared around 625 $cm^{-1}$, 875 $cm^{-1}$, 1475 $cm^{-1}$, a cluster of peaks between 1950 to 2350 $cm^{-1}$ and 3476 to 3742 $cm^{-1}$. The peak of absorption that appeared at 875 $cm^{-1}$ may be due to stretching vibration Zn–O. The peak centred around 1400 $cm^{-1}$ and 1600 $cm^{-1}$ can be attributed to the asymmetric and symmetric stretching mode of C=O. A cluster of peaks appeared between 1950 $cm^{-1}$ and 2350 $cm^{-1}$ in all samples, corresponding to the presence of $CO_2$ in air trapped on the surface of nanoparticles.[24] The peaks observed in the range of 3350–3750 $cm^{-1}$ corresponds to the O–H stretching vibration of water molecule indicates adsorption of moisture contents on the surface of the sample. A vibrational mode observed around 625 $cm^{-1}$ for the doped samples is recognized as metal-oxide (Mn–O or Co–O) modes and it confirms the successful inclusion Co/Mn ions into the ZnO lattice sites.[25,26] The obtained results from FTIR are in good agreement with XRD findings.

### 3.4 Raman spectroscopy

Raman spectroscopy has been employed to study the disorder-induced due to the inclusion of dopant in the host matrix and to detect the existence of defects in material. Fig. 3(b) shows

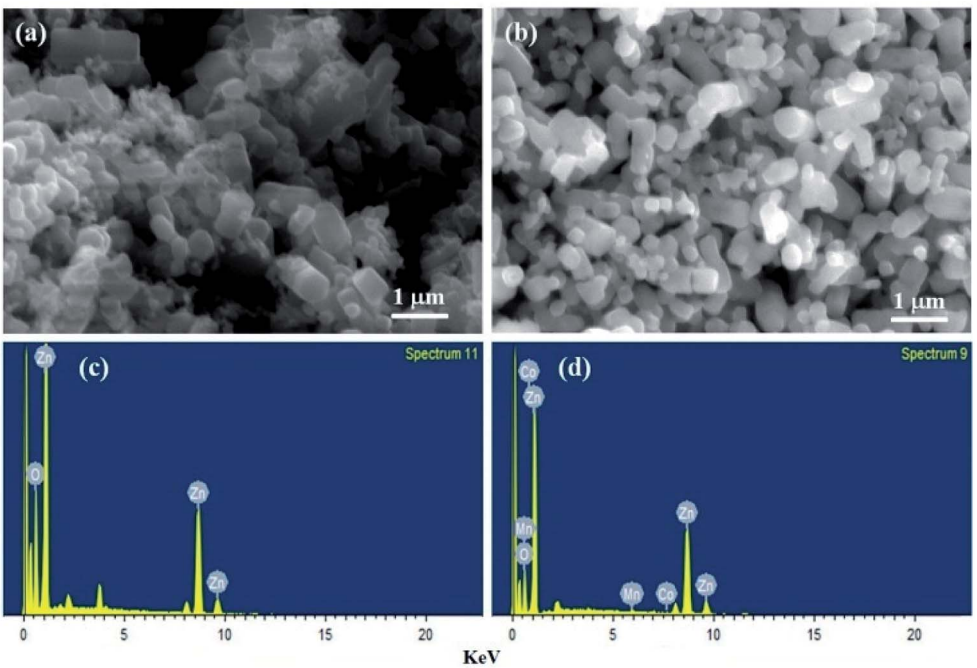


Fig. 2 SEM micrographs of (a) ZnO (b) 2% Mn and 6% Co doped ZnO nanoparticles. EDX spectra of (c) ZnO (d) 2% Mn and 6% Co doped ZnO nanoparticles.

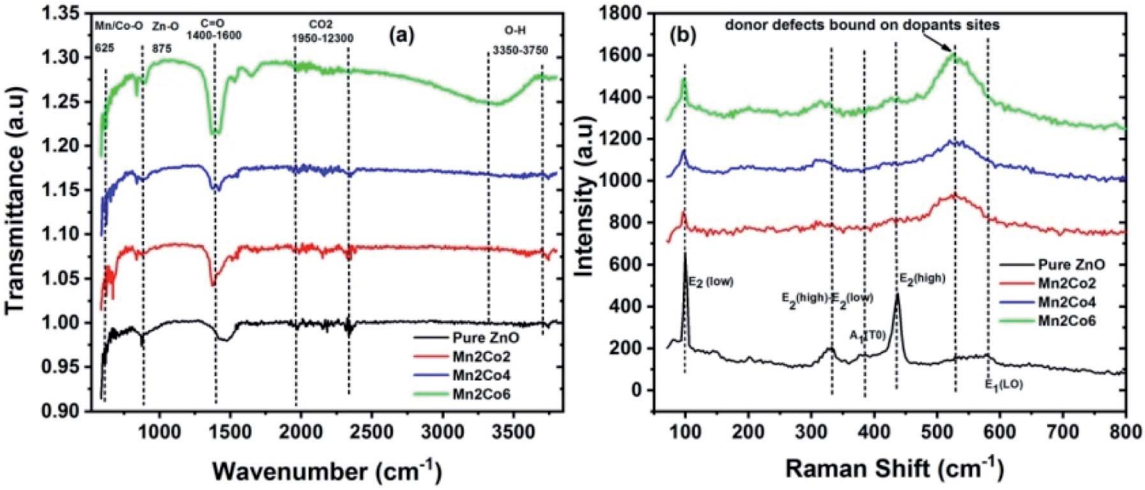


Fig. 3 (a) The FTIR spectra for pure ZnO, Mn2Co2, Mn2Co4, and Mn2Co6 nanoparticles at 300 K. (b) Raman spectra of ZnO and co-doped ZnO specimens.

a sharp and strong peak centred around 98 $cm^{-1}$ and 432 $cm^{-1}$ are due to the $E_2$ (low) and $E_2$ (high) phonon mode of ZnO respectively.[27] These peaks become broadened and their intensity decreases or vanishes with doping elements. Peak appeared around 331 and 380 $cm^{-1}$ is created due to multi phonon mode of $E_2$ (high)–$E_2$ (low) and A1(TO) respectively, which can be attributed to the single-crystalline nature of ZnO.[28] The intensities of these peaks decrease with doping, indicating that the inclusion of Mn/Co in the lattice may induce disorder in the system. A weak absorption peak at 580 $cm^{-1}$ corresponds to $E_1$ (LO) mode of vibration which is created due to oxygen vacancies. For the doped samples, a prominent feature peak appeared around 532 $cm^{-1}$ which can be ascribed to local vibration mode allied to Mn/Co that is coupled with donor defects like zinc interstitials and doubly ionized oxygen vacancies.[29]

### 3.5 Optical analysis

The optical properties of the samples have been investigated by UV-Vis spectrometer. Fig. 4(a) shows the UV-Vis absorption spectra at room temperature of pure ZnO and (Mn, Co) dual doped ZnO (Mn = 2% and Co = 2, 4 and 6%) nanoparticles. The absorbance spectra of (Mn, Co) dual doped ZnO shows a strong enhancement in the absorption of the visible region in comparison with the pure ZnO. This variation in the absorption can be related to size effects such as a shift in the average crystallite size, a disorder that occurs when the Mn and Co concentration increases, and the impurity levels induced by doping.[30] The pure ZnO shows an absorption edge at ~380 nm that shifts towards a higher wavelength ($\lambda$) (red-shift) for the doped samples. Along with the bandgap transition, other optical absorption features are observed for the Mn, Co doped ZnO samples in the $\lambda$ range 510–610 nm, as displayed in the inset of Fig. 4(a). This kind of absorption features has been shown in the optical absorption analysis of Mn and Co doped ZnO in the wavelength range (500–650 nm).[31] This kind of absorption behaviour is related to electronic transitions due to the existence of $Mn^{2+}$ and $Co^{2+}$ in a tetrahedral.[32,33] Given that the wurtzite structure of ZnO ($P6_3$/mmc space group) is formed of tetrahedral-coordinated $O^{2-}$ and $Zn^{2+}$ ions, the identification of this absorption signature in the visible region indicates the

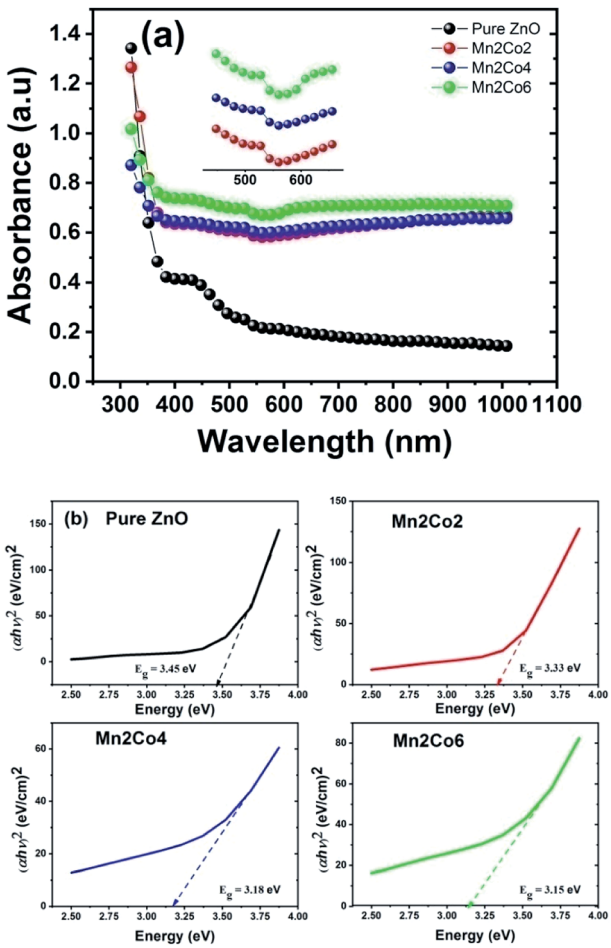


Fig. 4 (a) The UV-Vis absorption spectra for the pure and Mn/Co doped ZnO nanoparticles (b) calculation of energy band gap using Tauc plot method for all samples.

Table 2 Optical band gap values of ZnO and Mn/Co dual-doped ZnO nanostructures

| S. no. | Sample | Band gap (eV) |
|---|---|---|
| 1 | ZnO | 3.45 |
| 2 | Mn2Co2 | 3.33 |
| 3 | Mn2Co4 | 3.18 |
| 4 | Mn2Co6 | 3.15 |

efficient replacement of $Mn^{2+}$ and $Co^{2+}$ ions for the $Zn^{2+}$ positions in the ZnO host lattice.

The optical band gap ($E_g$) for the synthesized samples were calculated by Tauc relation given as[34]

$$\alpha h\nu = B(h\nu - E_g)^n \quad (4)$$

where $\alpha$ is the coefficient of optical absorption (calculated by relation $\alpha = 2.303 \times A/t$ where $A$ is the absorbance of the material and $t$ is the thickness of the cuvette), $B$ is a constant and $h\nu$ is the energy of the incident photon. The value of $n$ is assumed to be 1/2 since ZnO is a semiconductor with a straight bandgap. The energy gap could be calculated by extrapolating the linear portion of $(\alpha h\nu)^2$ against the $h\nu$ plots to the $x$-axis. The extrapolated curves of the synthesized pure and (Mn, Co) dual doped ZnO nanoparticles are shown in Fig. 4(b). The bandgap of pure ZnO is calculated as 3.45 eV, which is larger than the bulk value of ZnO. The calculated value of bandgap progressively decreases from 3.45 eV to 3.15 eV with doping of Mn = 2% and Co = 2, 4 and 6% in ZnO (Table 2). A decrease in energy the bandgap in various transition metal-doped ZnO was previously obtained by many researchers.[27,35] The enhancement in optical absorption and decrease in band gap of Mn/Co-doped ZnO is attributed to the increase in defects amount in the crystal structure compared to pure ZnO.[17] $Mn^{2+}/Co^{2+}$ incorporation in ZnO adds a tail state in the proximity of the valence band due to defect sites narrowing its energy gap. Thus, visible light's energy photon will be enough to excite electrons from the modified valence band to the conduction state.[36] Moreover, the observed reduction in bandgap with doping may originate from the exchange interaction between s–d and p–d band of localized d electron of $Mn^{2+}/Co^{2+}$ ions and 's' and 'p' electrons of the host Zn atom. The negative corrections of the conduction band and the positive corrections valence band may arise from the s–d and p–d exchange interaction; it would also lead to narrowing of the bandgap.[37] The decrease in energy in the bandgap of the doped sample can also be attributed to strong quantum confinements and an increase in surface-to-volume ratio.[38]

### 3.6 Dielectric properties

The measurement of dielectric constant *versus* frequency ($f$) at 300 K for the pure ZnO, Mn2Co2, Mn2Co4 and Mn2Co6 nanoparticles are depicted in Fig. 5(a). The dielectric properties were measured using an impedance analyzer (40 Hz $\leq f \leq 10^6$ Hz). The samples powder were pressed at 10 tons for 1 min into a circular shaped pellet of diameter 9 mm and thickness ~3 mm. The pellets were heated at 400 °C for 2 h to remove the porosity in the material. Both sides of the pellets were silver-pasted that acted as electrodes having the sample as the dielectric medium. A thin copper wire joined the electrodes in turn to serve as ohmic contacts. From the measurement of capacitance ($C$), dielectric loss ($\varepsilon''$) and the dimensions of the

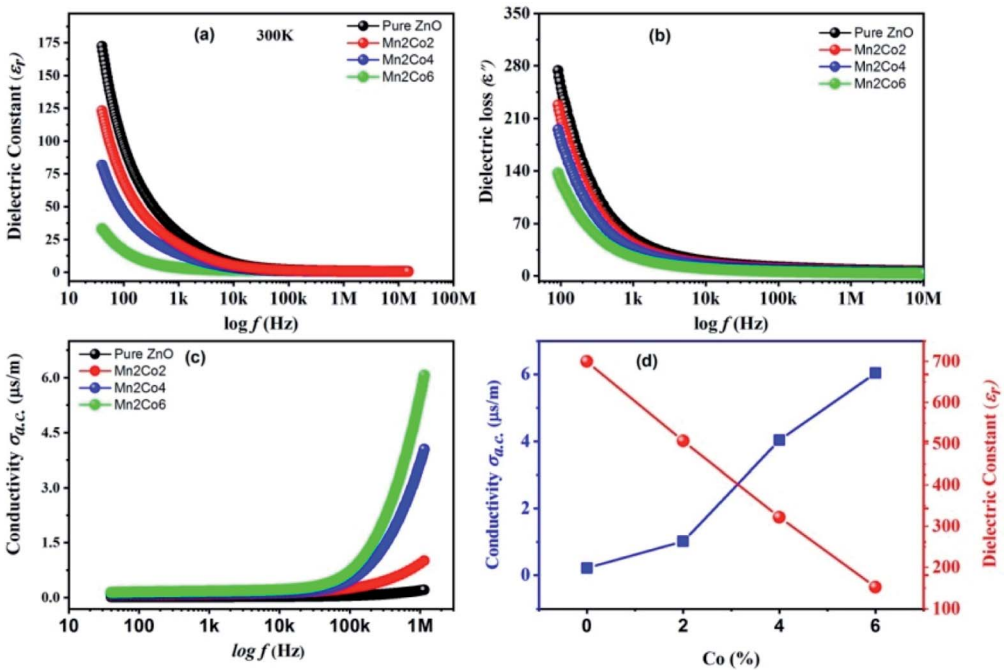


Fig. 5 Room temperature frequency-dependent variation for the pure ZnO, Mn2Co2, Mn2Co4 and Mn2Co6 nanoparticles in (a) $\varepsilon_r$, (b) $\varepsilon''$, (c) $\sigma_{ac}$, (d) $\sigma_{ac}$ and $\varepsilon_r$ *versus* Co concentration.

pellet (thickness and area), the dielectric constant ($\varepsilon_r$) and ac conductivity ($\sigma_{ac}$) were determined using eqn (5) and (6), respectively:[39]

$$\varepsilon_r = \frac{Cd}{\varepsilon_0 A} \quad (5)$$

$$\sigma_{ac} = \varepsilon_0 \varepsilon'' \omega \quad (6)$$

where $C$ denotes the capacitance, $\varepsilon_0$ refer to the permittivity of free space ($8.85 \times 10^{-12}$ $m^{-3}$ $kg^{-1}$ $s^4$ $A^2$), $d$ is the thickness of circular-shaped sample, and $A$ represents the pellet area in $m^2$ where $\omega = 2\pi f$ is the angular frequency.

The $\varepsilon_r$ *versus* $f$ for ZnO and co-doped ZnO reveals that the $\varepsilon_r$ decreases with the enhanced $f$ for all the specimens. At low $f$, an exponentially decreasing trend is observed; however, it becomes slow at high $f$, attaining a $f$-independent trend. The reduction in $\varepsilon_r$ with an increase in $f$ is expected behaviour for oxide-based nanoparticles.[24] All the $f$-dependent dielectric constant plots show a rapid decrease at lower $f$s, this grows steadily slower as $f$ increases until an almost-independent behaviour appears at higher $f$s. The showed higher values of $\varepsilon_r$ may be discussed by using Rotation dielectric polarization (RDP) and space charge polarization (SCP) mechanisms. The region at the interface restrains the considerable number of oxygen vacancies, vacancy clusters, immobilized radicals, *etc.* The single or double ionized vacancies are formed when these oxygen vacancies are ionized.[40] The randomly oriented combination of negative and positive vacancies constitutes a large dipole moment that can only be polarized in the presence of an external applied field.[41] These dipole moments will be field-aligned in the presence of an external field, resulting in RDP. Additionally, the moment of charges in the opposite direction of the electric field induces SCP and are trapped by a defect present at the interface of the nanostructure material. This SCP in the specimens produces large polarization at lower $f$s and enhanced dielectric constant due to electrically active grain boundaries.[42] At higher $f$, the $\varepsilon_r$ decreases with increasing $f$ because any component granting to polarizability is observed to lag behind the applied field. Beyond a particular $f$, dipoles and the alternating field are strongly mismatched finally; the dielectric constant receive a constant value; hence a $f$-independent dielectric response becomes visible.[43]

### 3.7 Dielectric loss

Fig. 5(b) illustrates the dielectric loss measurement $\varepsilon''$ (imaginary part of $\varepsilon_r$) *versus* $f$ at 300 K for the pure and Mn 2%, Co 2, 4 and 6% doped ZnO nanoparticles. The figure shows that the $\varepsilon''$ decreases sharply with increasing $f$ up to 1 kHz followed by a steady slow decrease. All the samples show similar activity, *i.e.*, low-$f$ dispersion behaviour and $f$-independent nature of dielectric loss at high $f$. The migration of ions in the material is ascribed to the decrease in $\varepsilon''$ in the low $f$s region.[41] Likewise, the behaviour of $\varepsilon''$ at low and intermediate fs can be attributed to ionic hopping, *i.e.* losses in conduction due to ion migration.[6] On the other hand, ion vibrations might be the only way for $\varepsilon''$ steady behaviour at high $f$s.[40]

### 3.8 Electrical conductivity

Fig. 5(c) shows the $f$-dependent $\sigma_{ac}$ for the pure and Mn, Co doped ZnO nanoparticles measured at room temperature. The $\sigma_{ac}$ enhances with rising $f$s, especially at high $f$s, which corresponds to the published results.[44] The enhancement in $\sigma_{ac}$ is negligible at low $f$s, showing a gradual increase with the increase in $f$s, finally showing a rapid increase in the conductivity in the higher $f$s region. The variation of $\varepsilon_r$ and $\sigma_{ac}$ as a function of Co doping is shown in Fig. 5(d). The hopping model can be used to explain the behaviour of conductivity.[24] The conductivity is steady in the low $f$s region; the transport occurs on infinite paths. However, in the high $f$s region, the transport takes place *via* the hopping of charge carriers. The hopping of charges between the charge carriers ions is enhanced by increasing $f$ of the applied field, which improves the mobility of carriers, thus leading to an increase in conductivity.[45] The undoped and (Mn,Co) doped ZnO specimens follow the following equation, $\sigma_{ac} = \varepsilon_0 \varepsilon'' \omega$, where $\omega = 2\pi f$. It is obvious from the equation that $\sigma_{ac}$ is $\varepsilon''$ dependent only. Hence, as the $\varepsilon''$ reduces with increase in $f$, it $\sigma_{ac}$ enhances. This result is well-consistent with literature, where it is revealed that the increase $\sigma_{ac}$ with the enhancement in $f$ is ascribed to the series resistance effect.[46] Actually, the increase in $\sigma_{ac}$ can be described by two possible mechanisms; one is the electric energy allied with the high $f$ can effectively promote the hopping of charge carriers between the nano-sized particles, and the second is owing to the improved dielectric relaxation of the polarization of ZnO nanostructure in the high-$f$ range.[47]

### 3.9 Magnetic properties

For practical spintronic application, the room temperature magnetic properties of DMS are important. Fig. 6(a) illustrates the magnetization hysteresis loops ($M$–$H$ loops) for Mn2Co2, Mn2Co4 and Mn2Co6 nanoparticles measured at 300 K. The pure ZnO sample display a diamagnetic response at 300 K as expected (the data is not shown here). It is evident from the figure that the FM behaviour was progressively enhanced for

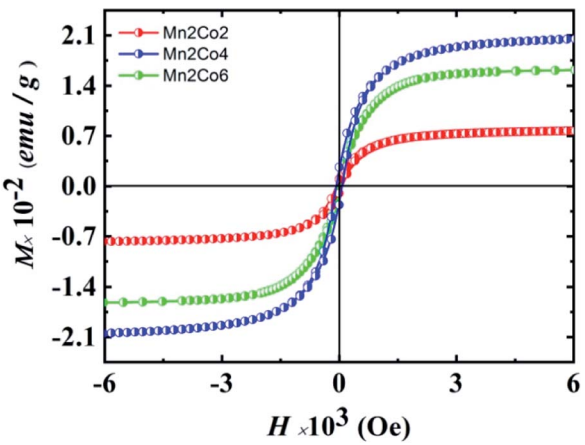


Fig. 6 $M$–$H$ curves for Mn 2% (fixed) and Co 2, 4, and 6% doped ZnO at room temperature.

Table 3 The magnetic properties parameters for all the doped samples

| Sample | Coercive field (Oe) | Remanent magnetization (emu $g^{-1}$) | Saturation magnetization (emu $g^{-1}$) |
|---|---|---|---|
| Mn2Co2 | 27 | 0.0014 | 0.038 |
| Mn2Co4 | 56 | 0.0027 | 0.101 |
| Mn2Co6 | 51 | 0.0022 | 0.080 |

Mn = 2% and Co = 2, 4% doped ZnO. However, the FM behaviour decremented for Mn = 2% and Co = 6% doped sample. The remanent magnetization ($M_r$) and coercive field ($H_c$) is also observed to enhance for Mn2Co2 and Mn2Co4; however, they decreased for Mn2Co6. A $H_c$ of 27 and 56 Oe was found for Mn2Co2, and Mn2Co4 samples, respectively and $M_r$ of 0.0014 and 0.0.027 emu/g was observed for Mn2Co2 and Mn2Co4, respectively (Table 3). The $H_c$ and $M_r$ subsequently decreased to 51 Oe and 0.0022 emu $g^{-1}$ correspondingly for heavily doped samples (Mn2Co6). When ZnO is heavily doped (Mn = 2 and Co = 6%), the ZnO lattice's rapid expansion and the FM ordering may be destroyed due to significant structural disorder.[40] The observed highest $M_r$ for 4% Co (Mn2Co4) is higher than that reported in the literature.[48]

The origin of RTFM in DMS is an open-ended question that may originate from many potential sources. The most likely contamination of CoO and MnO may come at the time of preparation. The CoO phase is antiferromagnetic with a Néel temperature of 293 K and hence cannot be the basis of RTFM.[49] MnO and its secondary phases $MnO_2$ and $Mn_2O_3$ are antiferromagnetic at room temperature.[50] Our XRD and Raman results show no phase related to MnO and CoO, signifying that ferromagnetism of (Mn, Co) dual doped ZnO is likewise inappropriate to the Mn and Co-associated phases. In oxides with a wide bandgap, the TM ions and the impurity bands hybridization are robustly linked to the TM 3d bands inside the bandgap affecting the magnetic behaviors.[51] The impurity band (oxygen vacancy, $V_O$) may fall into the split 3d major spin and minor spin states of (Mn, Co) dual doped ZnO. In the case of increasing $V_O$ content, the spin-up and spin-down state is unequal, causing unpaired electrons in the degenerated d-orbitals ($e_g$) of TM ions that cause an imbalance of electron distribution.[51,52] To keep the system charge-neutral, few oxygen ions leave from the lattice, leaving oxygen in the vicinity of Mn and Co doped ions. The electronic configuration for $Mn^{2+}$ ion is $3d^5 4s^0$; the three electrons of 3d level occupy the $t_{2g}$ state while the other two electrons reside in the $e_g$ state. $3d^7 4s^2$ is the electronic configuration of $Co^{2+}$ where its $e_g$ level is occupied with two electrons.[52] Theoretically, it is reported by Jorgensen *et al.* that oxygen vacancies can cause significant changes in the band structures of the parent oxides and might make contributions considerably to ferromagnetism.[53] Oxygen vacancies are best known as color centers (F centers) illustrate three different charge states, $F^{2+}$ as unoccupied corresponding to $V_0^{++}$, $F^+$ as singly occupied corresponding to $V_0^+$ and $F^0$ as doubly occupied corresponding to $V_O^\times$. $V_0^{++}$ and $V_O^\times$ do not contribute to the ferromagnetism in ZnO because it is in zero spin ground states.[51] The $V_0^+$ carries a strongly localized trapped electron that induced bound magnetic polarons (BMP) and magnetic moment in DMSs.[54] The origin of ferromagnetism in our observed experiment results can be attributed to $V_0^+$ and $Mn^{2+}/Co^{2+}$ ions; $V_O$ electrons lying at the bottom of the gap interact with the many surrounding ions $Mn^{2+}$ and $Co^{2+}$, directing all spins, forming a BMP, thereby inducing ferromagnetic ordering. The BMPs overlap when the concentration of TM ions goes over a critical threshold leading to long-range ferromagnetism ordering.[52] Our investigation shows that in the Mn2Co4 sample, the simultaneous doping of Mn and Co into ZnO can increase the carrier concentration through oxygen vacancies, leading to enhanced RTFM.

## 4. Conclusions

Pure ZnO and Mn, Co doped ZnO nanoparticles with a fixed Mn content of 2% and varies Co substitution (2%, 4%, and 6%) were prepared by co-precipitation synthesis route. XRD characterization revealed that the nanoparticles crystallize in a hexagonal wurtzite structure with no extra phase present. The crystallite size was established to be (Mn, Co) doping depended and it increased in the doped samples compared to the pure ZnO. SEM analysis showed that the nanoparticles were spherical, and the required elements were present as confirmed by EDX analysis. The FTIR and Raman spectroscopy showed the wurtzite structure of ZnO nanoparticles and the vibration mode assigned to the bound of Mn/Co with the donor defects for the doped samples. The UV-Vis spectroscopy showed a red-shift for Mn/Co-doped ZnO. Furthermore, it revealed that dual doping in ZnO can be used to manipulate both optical absorption and bandgap of ZnO nanoparticles. Our study showed that dielectric constant and dielectric loss decremented with increasing doping and frequency whilst the electrical conductivity enhanced. Based on *M–H* measurements, we showed that room-temperature ferromagnetism could be induced in the (Mn, Co) doped samples, and its origin is attributed to bound magnetic polarons. Thus, our systematic study may contribute to advancing research on magneto-optical and spintronic materials based on Mn/Co dual doped ZnO nanostructures.

## Funding

This work was financially supported by Taif University with a Project number (TURSP-2020/228), Taif University, Taif, Saudi Arabia.

## Author contributions

Conceptualization, A. S., K. S., M. S. and R. K; data curation, A. S., M. S., Y. I. and N. A.; formal analysis, A. R. K., G. A., W. H. S., and K. A.; investigation, A. S., K. S., M. S., N. A. and R. K.; methodology, A. S., W. H. S., G. A. and K. A.; project administration, A. S., A. R. K., Y. I. and R. K.; resources, A. S., G. A., A. R. K., K. A.; software, A. S., N. A. and R. K.; supervision, A. S., Y. I., W. H. S., S. A. O. and R. K.; writing—original draft, A. S., A. R. K. and R. K.; writing – review and editing, A. S., K. S., W. H. S., G.

A., K. A., S. A. O. and R. K.; all authors have read and agreed to the published version of the manuscript.

## Conflicts of interest

There are no conflicts to declare.

## Acknowledgements

The authors appreciated Taif University Researchers Supporting Project number TURSP-2020/228, Taif University, Taif, Saudi Arabia.

## References

1 M. Y. Ali, M. Khan, A. T. Karim, M. M. Rahman and M. Kamruzzaman, *Heliyon*, 2020, **6**, e03588.
2 R. Sangeetha, S. Muthukumaran and M. Ashokkumar, *Spectrochim. Acta, Part A*, 2015, **144**, 1–7.
3 K. Karthika and K. Ravichandran, *J. Mater. Sci. Technol.*, 2015, **31**, 1111–1117.
4 K. C. Verma, in *Magnetic Materials and Magnetic Levitation*, IntechOpen, 2020.
5 A. B. Djurišić, X. Chen, Y. H. Leung and A. M. C. Ng, *J. Mater. Chem.*, 2012, **22**, 6526–6535.
6 R. Khan, C. I. L. de Araujo, T. Khan, S. A. Khattak, E. Ahmed, A. Khan, B. Ullah, G. Khan, K. Safeen and A. Safeen, *J. Mater. Sci.: Mater. Electron.*, 2019, **30**, 3396–3404.
7 K. C. Verma, in *Magnetic Materials and Magnetic Levitation*, IntechOpen, 2020, p. 109.
8 S. Sinha, M. Singh and R. Singh, *Int. J. Emerg. Res. Manag. Technol*, 2015, **4**, 16–20.
9 N. Lathiotakis, A. N. Andriotis and M. Menon, *Phys. Rev. B: Condens. Matter Mater. Phys.*, 2008, **78**, 193311.
10 D. Sharma and R. Jha, *Ceram. Int.*, 2017, **43**, 8488–8496.
11 H. Cao, P. Lu, N. Cai, X. Zhang, Z. Yu, T. Gao and S. Wang, *J. Magn. Magn. Mater.*, 2014, **352**, 66–71.
12 J. Beltrán, C. Barrero and A. Punnoose, *J. Phys. Chem. C*, 2016, **120**, 8969–8978.
13 G. Vijayaprasath, R. Murugan, S. Asaithambi, P. Sakthivel, T. Mahalingam, Y. Hayakawa and G. Ravi, *Ceram. Int.*, 2016, **42**, 2836–2845.
14 A. Kocyigit and R. Topkaya, *Mater. Res. Express*, 2019, **6**, 096116.
15 S. Das, A. Bandyopadhyay, P. Saha, S. Das and S. Sutradhar, *J. Alloys Compd.*, 2018, **749**, 1–9.
16 C. B. Ong, L. Y. Ng and A. W. Mohammad, *Renewable Sustainable Energy Rev.*, 2018, **81**, 536–551.
17 R. Ullah and J. Dutta, *J. Hazard. Mater.*, 2008, **156**, 194–200.
18 B. Yahmadi, O. Kamoun, B. Alhalaili, S. Alleg, R. Vidu and N. Kamoun Turki, *Nanomaterials*, 2020, **10**, 1507.
19 W. Li, G. Wang, C. Chen, J. Liao and Z. Li, *Nanomaterials*, 2017, **7**, 20.
20 R. K. Yadav and P. Chauhan, *Indian J. Pure Appl. Phys.*, 2020, **57**, 881–890.
21 R. Khan and S. Fashu, *J. Mater. Sci.: Mater. Electron.*, 2017, **28**, 10122–10130.
22 R. T. Da Silva, A. Mesquita, A. O. De Zevallos, T. Chiaramonte, X. Gratens, V. A. Chitta, J. M. Morbec, G. Rahman, V. M. Garcia-Suarez and A. C. Doriguetto, *Phys. Chem. Chem. Phys.*, 2018, **20**, 20257–20269.
23 P. Gu, X. Zhu and D. Yang, *RSC Adv.*, 2019, **9**, 8039–8047.
24 M. Zubair, A. Khan, T. Hua, N. Ilyas, S. Fashu, A. M. Afzal, M. A. Safeen and R. Khan, *J. Mater. Sci.: Mater. Electron.*, 2021, **32**, 9463–9474.
25 D. Kumbhar, S. Kumbhar, A. Dhodamani, S. Delekar, N. Harale, R. Nalawade and A. Nalawade, *Inorg. Nano-Met. Chem.*, 2021, **51**, 1258–1271.
26 G. Vijayakumar, G. Boopathi and M. Elango, *Mater. Technol.*, 2019, **34**, 807–817.
27 C. Belkhaoui, N. Mzabi, H. Smaoui and P. Daniel, *Results Phys.*, 2019, **12**, 1686–1696.
28 M. Almoussawi, A. Abdallah, K. Habanjar and R. Awad, *Mater. Res. Express*, 2020, **7**, 105011.
29 A. Chanda, S. Gupta, M. Vasundhara, S. R. Joshi, G. R. Mutta and J. Singh, *RSC Adv.*, 2017, **7**, 50527–50536.
30 W.-J. Qin, J. Sun, J. Yang and X.-W. Du, *Mater. Chem. Phys.*, 2011, **130**, 425–430.
31 K. J. Kim and Y. R. Park, *J. Appl. Phys.*, 2003, **94**, 867–869.
32 S. Deka and P. Joy, *Solid State Commun.*, 2007, **142**, 190–194.
33 M. Patra, K. Manzoor, M. Manoth, S. Vadera and N. Kumar, *J. Phys. Chem. Solids*, 2009, **70**, 659–664.
34 K. Safeen, V. Micheli, R. Bartali, G. Gottardi, A. Safeen, H. Ullah and N. Laidani, *Mod. Phys. Lett. B*, 2019, **33**, 1950313.
35 M. Ahmad, E. Ahmed, Y. Zhang, N. Khalid, J. Xu, M. Ullah and Z. Hong, *Curr. Appl. Phys.*, 2013, **13**, 697–704.
36 E. Pragna, M. Ramanadha, A. Sudharani and K. S. Kumar, *J. Supercond. Novel Magn.*, 2021, 1–10.
37 S. D. Birajdar, P. P. Khirade, V. Bhagwat, A. V. Humbe and K. Jadhav, *J. Alloys Compd.*, 2016, **683**, 513–526.
38 C. Mrabet, O. Kamoun, A. Boukhachem, M. Amlouk and T. Manoubi, *J. Alloys Compd.*, 2015, **648**, 826–837.
39 G. Asghar, S. Asri, S. N. Khusro, G. H. Tariq, M. Awan, M. Irshad, A. Safeen, Y. Iqbal, W. H. Shah and M. Anis-ur-Rehman, *J. Electron. Mater.*, 2020, **49**, 4318–4323.
40 K. Rajwali and F. Ming-Hu, *Chin. Phys. B*, 2015, **24**, 127803.
41 N. Grimes and R. W. Grimes, *J. Phys.: Condens. Matter*, 1998, **10**, 3029.
42 R. Khan, S. Fashu and M.-U. Rahman, *J. Mater. Sci.: Mater. Electron.*, 2016, **27**, 7725–7730.
43 R. Khan, S. Fashu and Y. Zaman, *J. Mater. Sci.: Mater. Electron.*, 2016, **27**, 5960–5966.
44 J. V. Siva, S. K. Tripathy and R. A. Ramalingeswara, *J. Electron. Mater.*, 2020, **49**, 3540–3554.
45 N. Mazumder, A. Bharati, S. Saha, D. Sen and K. Chattopadhyay, *Curr. Appl. Phys.*, 2012, **12**, 975–982.
46 O. Pakma, N. Serin, T. Serin and Ş. Altındal, *J. Phys. D: Appl. Phys.*, 2008, **41**, 215103.
47 C.-H. Ho, C.-D. Liu, C.-H. Hsieh, K.-H. Hsieh and S.-N. Lee, *Synth. Met.*, 2008, **158**, 630–637.
48 M. Shatnawi, A. Alsmadi, I. Bsoul, B. Salameh, G. Alna'washi, F. Al-Dweri and F. El Akkad, *J. Alloys Compd.*, 2016, **655**, 244–252.

49 A. Mandziak, G. D Soria, J. E. Prieto, P. Prieto, C. Granados-Miralles, A. Quesada, M. Foerster, L. Aballe and J. de la Figuera, *Sci. Rep.*, 2019, **9**, 1–8.
50 T.-L. Phan and S. Yu, *J. Phys. Chem. C*, 2013, **117**, 6443–6453.
51 J. Coey, M. Venkatesan and C. Fitzgerald, *Nat. Mater.*, 2005, **4**, 173–179.
52 Q. Gao, Y. Dai, B. Han, W. Zhu, X. Li and C. Li, *Appl. Surf. Sci.*, 2019, **490**, 178–187.
53 J. Jorgensen, B. Veal, W. Kwok, G. Crabtree, A. Umezawa, L. Nowicki and A. Paulikas, *Phys. Rev. B: Condens. Matter Mater. Phys.*, 1987, **36**, 5731.
54 H. Ji, C. Cai, S. Zhou and W. Liu, *J. Mater. Sci.: Mater. Electron.*, 2018, **29**, 12917–12926.